

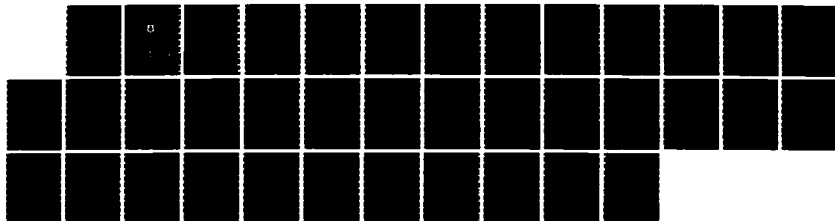
AD-A173 364

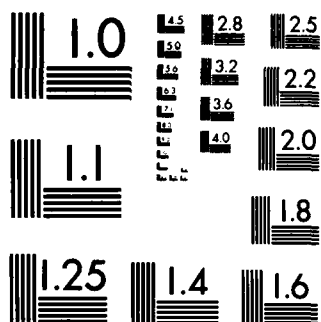
ACTA AERONAUTICA ET ASTRONAUTICA SINICA (SELECTED
ARTICLES)(U) FOREIGN TECHNOLOGY DIV WRIGHT-PATTERSON
AFB OH 0 ZHENHAN ET AL 02 OCT 86 FTD-ID(RS)T-0777-86
F/G 20/4

1/1

UNCLASSIFIED

NL





XEROCOPY RESOLUTION TEST CHART
NATIONAL BUREAU OF STANDARDS-1963-A

FOREIGN TECHNOLOGY DIVISION



ACTA AERONAUTICA ET ASTRONAUTICA SINICA
(Selected Articles)



DTIC
ELECTE
OCT 22 1986
S D
E

DTIC FILE COPY

Approved for public release;
Distribution unlimited.



HUMAN TRANSLATION

FTD-ID(RS)T-0777-86

2 October 1986

MICROFICHE NR: FTD-86-C-002261

ACTA AERONAUTICA ET ASTRONAUTICA SINICA
(Selected Articles)

English pages: 30

Source: Hong Kong Xuebao, Vol. 7, Nr. 1, February 1986,
pp. 11-18; 104-107; 114-118

Country of origin: China

Translated by: FLS, INC.

F33657-85-D-2079

Requester: FTD/TQTA

Approved for public release; Distribution unlimited.

THIS TRANSLATION IS A RENDITION OF THE ORIGINAL FOREIGN TEXT WITHOUT ANY ANALYTICAL OR EDITORIAL COMMENT. STATEMENTS OR THEORIES ADVOCATED OR IMPLIED ARE THOSE OF THE SOURCE AND DO NOT NECESSARILY REFLECT THE POSITION OR OPINION OF THE FOREIGN TECHNOLOGY DIVISION.

PREPARED BY:

TRANSLATION DIVISION
FOREIGN TECHNOLOGY DIVISION
WPAFB, OHIO.

TABLE OF CONTENTS :

1. Application of Harmonic Analysis Method to Research on Rotor Airloads, by Qin Zhenhan..... ii

2. Some Problems in the Finite-Difference Computation of Three-Dimensional Transonic Flows, by Chen Tiemin..... 11

3. Numerical Computation of the Three-Dimensional Viscous Interference Flow Field of a Vertical Jet in a Crossflow, by Pan Huachen and Zhang Shiyong..... 21

Accession For	
NTIS GRA&I	<input checked="" type="checkbox"/>
DTIC TAB	<input type="checkbox"/>
Unannounced	<input type="checkbox"/>
Justification	
By _____	
Distribution / _____	
Availability Codes	
Dist _____	Special _____
A-1	



APPLICATION OF HARMONIC ANALYSIS METHOD TO RESEARCH ON ROTOR AIRLOADS

Qiu Zhenhan

(Chinese Helicopter Research and Development Institute)

Abstract

According to the rotor vortex theory, the rotor circulation and the rotor induced velocity are developed into Fourier series. The circulation distribution along blade spanwise is expressed in Terms of segment-by-segment linear functions. In consequence the induced velocity equations and the circulation equations are derived. The engineering application of the rotor vortex theory is provided. Then the induced velocity and its harmonic components are obtained to provide a quantitative basis for the vortex model. For calculating each order harmonic components of the induced velocity a simplified method is put forward which considers the effects of each order circulation with neglecting those of higher order. The method saves the computer time and is of significant benefit.

GRAPHICS DISCLAIMER

All figures, graphics, tables, equations, etc. merged into this translation were extracted from the best quality copy available.

APPLICATION OF HARMONIC ANALYSIS METHOD TO RESEARCH ON ROTOR AIRLOADS

Qin Zhenhan
Chinese Helicopter Research and Development Institute

Submitted 31 July 1984

This paper uses the rotor vortex theory of Professor Wang Shichuen as a basis to develop the rotor circulation and induced velocity into Fourier series. The circulation distribution along blade spanwise is expressed in terms of segment-by-segment linear functions and the linear equations for calculating rotor airloads using the circulation as the unknown are derived. This has resolved the practical application problems of the rotor vortex theory that for many years have not been able to be resolved.

I. Preface

There have been many theories and articles on the aerodynamic calculations of helicopter rotor-blades, and among which is the rotor vortex theory of the stationary vortex system of Professor Wang Shicun^[1]. But it requires proper modifications when applying this theory to engineering calculations. Due to the limitation of resources in the past, the rotor-blade could only be treated

as a rigid blade, and this is obviously improper. As the application of computer develops in our country, the elastic deformation (bending, twisting, etc.) of the rotor-blade can be considered simultaneously and this can more truthfully reflect the rotor characteristics.

According to Reference [1], this paper develops the rotor circulation and induced velocity into the Fourier series. This manipulation makes the physical significance between the circulation and its related parameters become very clear and is rather conducive toward the understanding of the vortex model and the effects of various vortex systems. Although the mathematical manipulations are quite complex, a smaller computer capacity is required. While high accuracy computations can be conducted on a computer with large capacity, results can also be obtained using a computer with small capacity. For example, it only requires half an hour to obtain results that meet engineering requirements on the DJS-21 computer which only processes ten-thousand operations per second. Therefore, it is economical and suitable for engineering applications.

II. Induced Velocity Equations

According to Reference [1], the axial induced velocity at any point on the rotor hub can be developed into the Fourier series

$$v_p(\bar{r}) = v_{0p}(\bar{r}) + \sum_{n=1}^N [v_{ncp}(\bar{r}) \cos n\psi + v_{nsp}(\bar{r}) \sin n\psi] \quad (1)$$

where $v_{0p}(\bar{r}) = v_{r0} + v_{z0} + v_{H0}$; $v_{ncp}(\bar{r}) = v_{rnc} + v_{znc} + v_{Hnc}$; $v_{nsp}(\bar{r}) = v_{rns} + v_{zns} + v_{Hns}$.

Here every induced velocity is agitated by the circulation which consists of attached vortex, vertical free vortex and horizontal free vortex.

According to Reference [2], if the circulation distribution along spanwise is expressed in terms of segment-by-segment linear functions, the induced velocity derived from vertical free vortex can be expressed as

$$v_z = v_{z_0} + \sum_{n=1}^N (v_{z_{0n}} \cos n\psi + v_{z_{1n}} \sin n\psi) \quad (2)$$

where

$$\begin{aligned} v_{z_0} = & -K_v \Gamma_0(\bar{r}) + \sum_{m=1}^N \left\{ \sum_{t=1}^{p-1} [(C_{13}(m)C_{113}/\bar{r})\Delta\Gamma_{mt} + (C_{16}(m)C_{116} \right. \\ & - C_{18}(m)C_{118})\Delta\Gamma_{mt}]/\delta_t + \sum_{t=p}^{NN} [(C_{14}(m)C_{114}/\bar{r})\Delta\Gamma_{mt} \\ & \left. + C_{17}(m)(C_{117} - C_{113})\Delta\Gamma_{mt}]/\delta_t \right\} \\ v_{z_{0n}} = & \sum_{t=1}^{p-1} (E_i C_{i10} \Delta\Gamma_0 - (1/2)K_v C_{i10} \Delta\Gamma_{nt} + (E_i C_{i12}/\bar{r})\Delta\Gamma_{nt})/\delta_t \\ & + \sum_{t=p}^{NN} [(1/2)K_v C_{i17} \Delta\Gamma_{nt} - E_i C_{i11} \Delta\Gamma_0 + (E_i C_{i13}/\bar{r})\Delta\Gamma_{nt}]/\delta_t \\ & + \sum_{m=1}^N \left\{ \sum_{t=1}^{p-1} [(C_2(m)C_{119} + C_3(m)C_{120})\Delta\Gamma_{mt} - (C_6(m)C_{123}/\bar{r})\Delta\Gamma_{mt}]/\delta_t \right. \\ & \left. + \sum_{t=p}^{NN} [(C_8(m)C_{121} + C_7(m)C_{122})\Delta\Gamma_{mt} - (C_{11}(m)C_{124}/\bar{r})\Delta\Gamma_{mt}]/\delta_t \right\} \\ v_{z_{1n}} = & \sum_{t=1}^{p-1} [(E_s C_{s10}/\bar{r})\Delta\Gamma_0 - (1/2)K_v C_{s10} \Delta\Gamma_{nt} + (E_s C_{s12}/\bar{r})\Delta\Gamma_{nt}]/\delta_t \\ & + \sum_{t=p}^{NN} [(E_s C_{s13}/\bar{r})\Delta\Gamma_0 + (1/2)K_v C_{s17} \Delta\Gamma_{nt} + (E_s C_{s15}/\bar{r})\Delta\Gamma_{nt}]/\delta_t \\ & + \sum_{m=1}^N \left\{ \sum_{t=1}^{p-1} [(C_2(m)C_{119} + C_4(m)C_{120})\Delta\Gamma_{mt} - (C_{10}(m)C_{123}/\bar{r})\Delta\Gamma_{mt}]/\delta_t \right. \\ & \left. + \sum_{t=p}^{NN} [(C_8(m)C_{121} + C_5(m)C_{122})\Delta\Gamma_{mt} - (C_{12}(m)C_{124}/\bar{r})\Delta\Gamma_{mt}]/\delta_t \right\} \end{aligned}$$

where $K_v = h/(4\pi V_1)$, $\Delta\Gamma = \Gamma_{t+1} - \Gamma_t$, $\delta_t = \bar{r}_{t+1} - \bar{r}_t$

E_i and $C_j[m]$ are the quantities related to K_v and the harmonic order number m and n . For example

$$\begin{aligned} E_1 &= K_v n C^n \\ C_1(m) &= \{C^n \{(2-m-n)/2\}_{m-1} + \delta C^{-n} \{(2+n-m)/2\}_{m-1}\} \\ &\quad \times C^n K_v / (2(m-1)!) \end{aligned}$$

where $C = (1 - \sin|\alpha_i|)/\cos|\alpha_i|$

C_{jk} is the quantity related to the integration of the super geometrical function [3]

$$C_j(t, l, \alpha, \beta, \bar{r}, 0) = \int_{\rho_0}^{\rho_1} (\bar{\rho}/\bar{r})^l F(\alpha, \beta, \gamma, (\bar{\rho}/\bar{r})^2) d\bar{\rho}$$

For example

$$C_{113} = C_j(t, m, (m+1)/2, (m+1)/2, \bar{r}, 0)$$

The expressions of induced velocities v_F and v_H agitated by the attached vortex and horizontal free vortex are similar to Equation (2).

III. Circulation Equations

According to Reference [2], the circulation is developed into Fourier series

$$\Gamma = \Gamma_0 + \sum_{m=1}^N (\Gamma_{m-} \cos m\psi + \Gamma_{m+} \sin m\psi) \quad (3)$$

where

$$\begin{aligned} \Gamma_0 &= (a_- \bar{b}/2) \left\{ v_0 + \bar{r}(\phi_0 + \phi_\Delta) + (\mu/2)\phi_2 + \lambda_0 \right. \\ &\quad \left. + \sum_{j=0}^{j_1} \{ K[(\mu/2)b_j^i - \bar{r}a_0^i] dy^i(\bar{e})/d\bar{r} + (\mu/2)a_j^i dy^i(\bar{r})/d\bar{r} \} \right\} \\ \Gamma_{m-} &= (a_- \bar{b}/2) \left\{ v_{m-} + \sum_{j=0}^{j_1} \left\{ K[\bar{r}a_m^i + (\mu/2)(b_{m-1}^i - b_{m+1}^i)] dy^i(\bar{e})/d\bar{r} \right. \right. \\ &\quad \left. \left. + (\mu/2)(a_{m-1}^i + a_{m+1}^i) dy^i(\bar{r})/d\bar{r} + mb_{m-}^i y^i(\bar{r}) \right\} \right\} \\ \Gamma_{m+} &= (a_- \bar{b}/2) \left\{ v_{m+} + \sum_{j=0}^{j_1} \left\{ K[\bar{r}b_m^i + (\mu/2)(a_{m-1}^i - a_{m+1}^i)] dy^i(\bar{e})/d\bar{r} \right. \right. \\ &\quad \left. \left. + (\mu/2)(b_{m-1}^i + b_{m+1}^i) dy^i(\bar{r})/d\bar{r} - ma_{m+}^i y^i(\bar{r}) \right\} \right\} \end{aligned}$$

The circulation distribution along spanwise is expressed in terms of segment-by-segment linear functions, then the circulation equation in the form of Γ_{op} is

$$\begin{aligned}
& \Gamma_{0s}/A_s + v_{0s} + \sum_{i=1}^{NN} \sum_{j=0}^{j1} \left\{ \mu (\bar{r}B_{2i} - \mu K/2) dy'(\bar{e})/d\bar{r} a_i^2 T_{1i}^j \Gamma_{1s} \right. \\
& + \left\{ (\mu/2) \bar{r} B_{1i}^j a_i^2 T_{1i}^j - (\bar{r} B_{1i}^j + (\mu/2) dy'(\bar{r})/d\bar{r}) a_i^2 T_{1i}^j \right\} \Gamma_{1s} \\
& + \left\{ (\mu/2) \bar{r} B_{2s} a_i^2 T_{1i}^j - (\mu K/2 - \bar{r} B_{2s}) a_i^2 T_{1i}^j \right\} dy'(\bar{e})/d\bar{r} \Gamma_{1s} \\
& + \left\{ (\mu/2) (\mu K/2 - \bar{r} B_{2s}) a_i^2 T_{1i}^j - \bar{r} B_{2s} a_i^2 T_{1i}^j \right\} dy'(\bar{e})/d\bar{r} \Gamma_{1s} \\
& + \left\{ \bar{r} B_{1i}^j a_i^2 T_{1i}^j - (\mu/2) (\bar{r} B_{1i}^j + (\mu/2) dy'(\bar{r})/d\bar{r}) a_i^2 T_{1i}^j \right\} \Gamma_{2s} \\
& \left. - (\mu/2) \bar{r} B_{1i}^j a_i^2 T_{1i}^j \Gamma_{2s} - (\mu/2) \bar{r} B_{2s} dy'(\bar{e})/d\bar{r} a_i^2 T_{1i}^j \Gamma_{2s} \right\} \\
& = \bar{r} B_{0s} + \Delta \Phi \bar{r}^2 + \mu \theta_s/2 + \lambda_s + \bar{r} B_{rs} C_r / (8\lambda K_s) \quad (4)
\end{aligned}$$

where $A_s = a_s \bar{b}/2$, $K_s = h/(4\pi)$,

$$\begin{aligned}
B_{1i}^j &= B_{1i} \int_{r_i}^1 y^j d\bar{r} - B_{2i} (1 - \bar{r}_i y^j(\bar{r})), \quad B_{2i}^j = B_{2i} (1 - y^j(\bar{r}_i)), \\
T_{1s}^j &= \begin{cases} (\bar{r}_2 Y_{1s}^{j,1} - Y_{1s}^{j,(s+1),1})/\delta_1 & i=1 \\ (\bar{r}_{i+1} Y_{1s}^{j,i} - Y_{1s}^{j,(s+1),i})/\delta_i + (Y_{1s}^{j,(s+1),(i-1)} - \bar{r}_{(i-1)} Y_{1s}^{j,(i-1)})/\delta_{i-1} & 2 \leq i \leq N_s \\ (Y_{1s}^{j,(s+1),N_s} - \bar{r}_{N_s} Y_{1s}^{j,N_s})/\delta_{N_s} & i = N_s + 1 \end{cases} \\
Y_{1s}^j &= \int_{r_i}^{r_{i+1}} y^j \bar{\rho}^{s-1} d\bar{\rho}
\end{aligned}$$

B_{ns} is the quantity related to B_0 , B_s and motion parameters. For example $B_{1s} = \mu (B_0 + B_s) / \{ 2 ((B_0/3)(1 - \bar{r}_1^3) + (\mu^2/2)(1 - \bar{r}_1)B_s) \}$

where $B_0 = 1/(1 + A_s K_s)$, $B_s = 1/(1 + A_s K_s (1 + C^2))$

Γ_{10s} , Γ_{1s} and other circulation equations can be derived accordingly.

IV. Rotor-Blade Airloads

Each order harmonic component of circulation can be obtained from the linear algebraic equations with circulation as the unknown which are derived by substituting the induced velocity equations into the circulation equations. According to the Zhukovskiy formula, the airloads per unit rotor-blade length are:

$$dT_{1i}/d\bar{r} = (\rho R^2/m_i)(W_{0s} \Gamma) \quad (5)$$

where

$$W_s = \bar{r} + \mu \sin \psi, \quad m_1 = \text{mass of one blade}; \quad \Gamma = \Gamma_0 + \sum_{m=1}^N (\Gamma_{m,c} \cos m\psi + \Gamma_{m,s} \sin m\psi)$$

Thus, the expressions of each order airloads per unit rotor-blade length are obtained; and therefore the airloads are obtained.

$$\begin{aligned} (dT_i/d\bar{r})_0 &= (\rho R^2/m_1) (\bar{r}\Gamma_0 + (\mu/2)\Gamma_{1,c}) \\ (dT_i/d\bar{r})_{1,c} &= (\rho R^2/m_1) (\bar{r}\Gamma_{1,c} + (\mu/2)\Gamma_{2,c}) \\ (dT_i/d\bar{r})_{1,s} &= (\rho R^2/m_1) (\mu\Gamma_0 + \bar{r}\Gamma_{1,s} - (\mu/2)\Gamma_{2,s}) \\ (dT_i/d\bar{r})_{m,c} &= (\rho R^2/m_1) (\bar{r}\Gamma_{m,c} + (\mu/2)(\Gamma_{(m+1),c} - \Gamma_{(m-1),c})) \\ (dT_i/d\bar{r})_{m,s} &= (\rho R^2/m_1) (\bar{r}\Gamma_{m,s} + (\mu/2)(\Gamma_{(m-1),s} - \Gamma_{(m+1),s})) \end{aligned}$$

V. Examples and Discussions

Numerical computations were conducted using the H-34 helicopter as an example. The calculated values were compared with the measured values during actual flight and the results are satisfactory; see Figs. 1 and 2.

Another helicopter with takeoff weight of 14,400 kg and rotor diameter f 21.3 m was used as an example to calculate each component of the induced velocity and obtain the curves of the azimuthal variation of total axial induced velocity (Fig. 3). Due to the limitation in space, only the second order components of the induced velocities which are agitated by separate harmonic components of attached vortex, vertical free vortex and horizontal free vortex, are given. See Table 1-3. The obtained harmonic components of the induced velocities have not yet been seen in any references. They provide a quantitative basis for the analysis and research of the vortex model.

It is very beneficial to perform example computations when only considering the same order induced velocity which is agitated by each order harmonic circulation before the same order, as shown in Fig. 4. If only the shaded areas are considered, comparison between the obtained results and the effects to the induced velocity when the total circulation is considered shows that their numerical values are very close; see Fig. 5. The computation time, however, is greatly reduced. The higher the order considered, the more distinctive the effect of reduction of computation time.

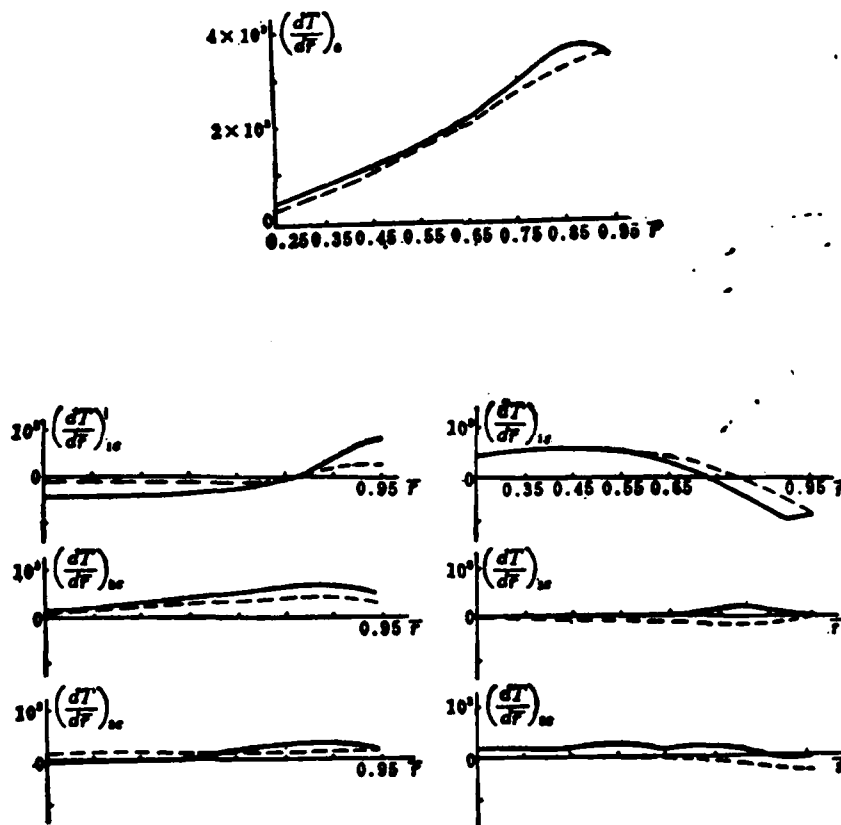


Fig. 1. Comparison of the harmonic components of dT/dF (N/m) at $\mu = 0.2$
 — test, ---- Calculation.

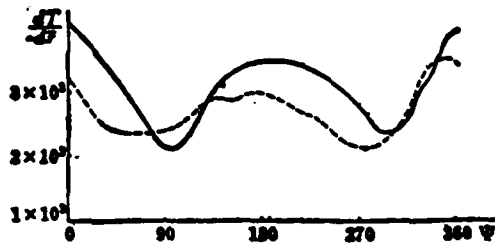


Fig. 2. Comparison of the azimuthal variation of $dT/d\psi$ (N/m) at $\mu = 0.2$, for $F = 0.75$
 — test, ---- calculation.

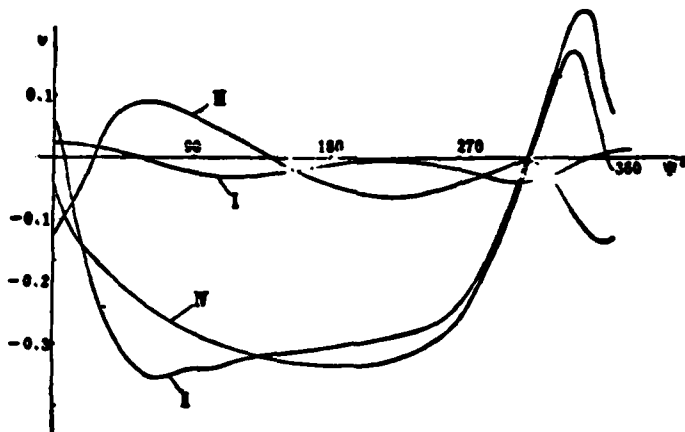


Fig. 3. Azimuthal variation of the induced velocity v at $\mu = 0.30$, for $F = 0.75$
 I — The induced velocity v_p by bound vortices; II — The induced velocity v_z by longitudinal vortices;
 III — The induced velocity v_H by lateral vortices; IV — Total induced velocity.

Table 1 The harmonic components of the induced velocity v_p

F	v_{p0}	$v_{p1_0} \times 10^{-3}$	$v_{p1_1} \times 10^{-3}$	$v_{p2_0} \times 10^{-3}$	$v_{p2_1} \times 10^{-3}$
0.25	0	-0.998	-0.250	0.462	0.694
0.35	0	-0.283	0.0318	0.937	0.995
0.45	0	0.423	0.126	0.855	0.749
0.55	0	0.553	0.113	0.764	0.629
0.65	0	0.601	0.0925	0.665	0.518
0.75	0	0.588	0.0719	0.558	0.414
0.85	0	0.513	0.0538	0.433	0.311
0.95	0	0.418	0.0448	0.338	0.245

Table 2 The harmonic components of the induced velocity v_z

F	$v_{z0} \times 10^{-1}$	$v_{z1_0} \times 10^{-1}$	$v_{z1_1} \times 10^{-2}$	$v_{z2_0} \times 10^{-2}$	$v_{z2_1} \times 10^{-2}$
0.25	-0.0827	0.104	-0.502	0.0535	-0.0578
0.35	-0.124	0.163	-0.933	0.396	-0.360
0.45	-0.186	0.167	-0.922	0.680	-0.533
0.55	-0.212	0.133	-0.811	0.760	-0.564
0.65	-0.233	0.138	-0.660	0.808	-0.569
0.75	-0.250	0.118	-0.474	0.830	-0.545
0.85	-0.283	0.0942	-0.258	0.833	-0.479
0.95	-0.268	0.0759	-0.146	0.832	-0.399

Table 3 The harmonic components of the induced velocity v_H

μ	$v_{H0} \times 10^{-2}$	$v_{H1c} \times 10^{-2}$	$v_{H1s} \times 10^{-2}$	$v_{H2c} \times 10^{-2}$	$v_{H2s} \times 10^{-2}$
0.25	-0.242	0.538	-0.572	-0.171	0.00510
0.35	-0.132	0.471	-0.280	-0.201	-0.000109
0.45	-0.0530	0.342	0.114	-0.240	0.0695
0.55	-0.0282	0.285	0.290	-0.257	0.122
0.65	-0.00967	0.231	0.450	-0.272	0.161
0.75	0.00296	0.179	0.592	-0.285	0.194
0.85	0.00959	0.130	0.715	-0.295	0.221
0.95	0.0167	0.109	0.768	-0.298	0.230

	Γ_0	Γ_{1c}	Γ_{1s}	Γ_{2c}	Γ_{2s}
v_0	hatched						
v_{1c}	hatched	hatched					
v_{1s}	hatched	hatched	hatched				
v_{2c}	hatched	hatched	hatched	hatched			
v_{2s}	hatched	hatched	hatched	hatched	hatched		
...	hatched	hatched	hatched	hatched	hatched	hatched	
...	hatched	hatched	hatched	hatched	hatched	hatched	hatched

Fig.4 Relation between the induced velocity and the Circulation in simplified calculation

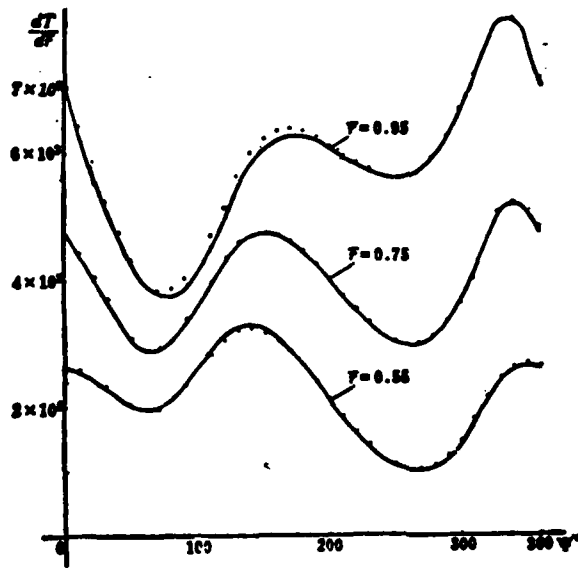


Fig.5 Variation of $dT/d\psi$ (N/m) with azimuth at $\mu = 0.27$
 —simplified circulation,total circulation.

(Xuie Zhenzhong and Duan Yuzhang took part in the work of this research subject).

REFERENCES

- [1] [U.S.S.R] Mili, et al. Computation and Design of Helicopter (vol. 1, Aerodynamics), National Defense Industry Publishing Company, (1977), p. 178.
- [2] Wang shicun, The Induced Velocity of Lift Rotor, Journal of Northwestern Industrial University, (1963) January.
- [3] Wang Zhuxi, Guo Duenren, Introduction of Special Functions, (1965), p. 152.
- [4] James Scheiman, A Tabulation of Helicopter Rotor-Blade Differential Pressures, Stresses and Motions as Measured in Flight, NASA TM X-952, Langley Research Center, Langley Station, Hampton, Va., December 11, (1964).

SOME PROBLEMS IN THE FINITE-DIFFERENCE COMPUTATION OF THREE-DIMENSIONAL TRANSONIC FLOWS

Chen Tiemin

(Beijing Institute of Aerodynamics)

Abstract

The mixed finite-difference relaxation iteration method is applied to calculation of the wing-body combination with rectangular wings based on the three-dimensional transonic small-disturbance potential equation in the cylinder coordinates. Meanwhile, the influences of different computation regions and relaxation parameters (on subsonic points) on the ranges of the computed Mach numbers, angles of attack and calculated results are studied.

It is shown that extending the computation region brings about increasing the convergence range of the small-disturbance equation, and the convergence rate and computation accuracy would be enhanced if the subsonic relaxation parameter is taken to be 1.9.

Also, it is demonstrated that the calculated results differ when the finite or infinite region is taken as the computation region of the r -direction. Particularly the distribution of the pressure coefficients near the wingtip varies obviously as the incident Mach number becomes larger.

SOME PROBLEMS IN THE FINITE-DIFFERENCE COMPUTATION OF THREE-DIMENSIONAL TRANSONIC FLOWS

Chen Tiemin
Beijing Institute of Aerodynamics

Submitted 25 January 1985

I. Introduction of Basic Method

1. Three-Dimensional Transonic Small-Disturbance Equation

The three-dimensional transonic small-disturbance equation in cylindrical coordinates is

$$A\varphi_{xx} + \varphi_{rr} + \frac{1}{r}\varphi_r + \frac{1}{r^2}\varphi_{\theta\theta} = 0 \quad (1)$$

where φ is disturbance potential; $A = \beta^2 - (\gamma + 1)M_\infty^2$, $\beta^2 = 1 - M_\infty^2$, γ is specific heat; M_∞ is the incident Mach number. If r-direction is selected as infinite region, through coordinate conversion $\eta = br/(1 + ar)$, the infinite region of r is converted to the finite computation region η . Here a and b are constants to be determined. Now Equation (1) can be rewritten as

$$A\varphi_{rr} + \frac{(b-a\eta)^2}{b} \left[\left(\frac{1}{\eta} - \frac{2a}{b} \right) \varphi_r + \frac{b-a\eta}{b} \varphi_{rr} \right] + \frac{(b-a\eta)^2}{\eta^2} \varphi_{\theta\theta} = 0 \quad (2)$$

Then Equations (1) and (2) correspond to the finite and infinite regions (select proper a and b values) of r respectively.

2. Boundary Conditions (See Fig. 1)

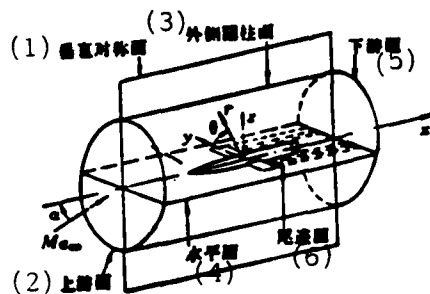


Fig. 1. Boundary surfaces and diagrammatic drawing of model
Key: (1) Vertical plane of symmetry; (2) Upstream plane; (3) Outer cylindrical surface; (4) Horizontal plane; (5) Downstream plane; (6) Tail-trace plane.

On the surface of the body: Assume the surface equation of the body symmetrical to the axes is $r=R(x)$, then the boundary condition of the tangential flow is

$$\lim_{r \rightarrow R} (r\varphi_r) = R(x)[R'(x) - \alpha \sin \theta] \quad (3)$$

where α is the incident attack angle.

On the surface of the wing: Assume the equations of upper and lower wing surfaces are $Z = f_{\pm}(x, y)$, then the flow along the upper and lower wing surfaces should satisfy

$$\lim_{\theta \rightarrow 0_{\pm}} (\varphi_{\theta}) = r [f'_{\pm}(x, y) - \alpha] \quad (4)$$

Here $f'_{\pm}(x, y) = \partial f_{\pm}(x, y) / \partial x$, 0_{\pm} represents the upper and lower wing surfaces.

On the tail-trace surface: It is known from the Kutta condition that

$$\varphi(x, y, 0_{+}) - \varphi(x, y, 0_{-}) = \Gamma(y) \quad (5)$$

There are two conditions on the upstream plane and the outer cylindrical surface:

(1) If Equation (1) is used, it should satisfy, from the solutions of small-disturbance wing lift problems,

$$\varphi(\Gamma) = \frac{\sin \theta}{4\pi r} \left(1 + \frac{x}{\sigma}\right) \int_{-s}^s \Gamma(y) dy \quad (6)$$

where $\sigma = \sqrt{x^2 + \beta^2 r^2}$, s is half of the span length.

(2) If Equation (2) is used, the disturbance potential is 0, i.e.,

$$\varphi = 0 \quad (7)$$

There are also two conditions on the downstream plane:

(1) If Equation (1) is used, should satisfy

$$\varphi(\Gamma) = \frac{r \sin \theta}{4\pi} \left(1 + \frac{x}{\sigma} \right) \int_{-s}^s \frac{\Gamma(y)}{\rho} dy \quad (8)$$

where

$$\rho = \sqrt{r^2 - 2ry \cos \theta + y^2}.$$

(2) If Equation (2) is used, the disturbance velocity

$$\varphi_r = 0 \quad (9)$$

3. Finite-Difference Formula, Finite-Difference Equation and Their Solutions

This paper uses the variable mixed finite-difference formula of Murman-Cole, i.e., φ_{xx} at subsonic point uses central finite-difference; at supersonic point uses incident finite-difference; r (or η) and θ -direction both use central finite-difference. The finite-difference formula at special point (with boundary conditions substituted):

(1) According to boundary condition (3), it can be obtained on the surface of the body that:

$$\frac{1}{r} (r\varphi_r) \Big|_{i,j,k} = \frac{1}{r_i \Delta r_i} \left[\frac{2r_i + \Delta r_i}{2} \cdot \frac{\varphi_{i,j,k+1} - \varphi_{i,j,k-1}}{\Delta r_i} - R(R' - \alpha \sin \theta) \right] \quad (10)$$

(2) On the upper and lower wing surfaces

$$\begin{cases} (\varphi_{\theta\theta})_{i,j,k} = \frac{2}{\Delta \theta_0} \left[\frac{\varphi_{i,j,l} - \varphi_{i,j,l+1}}{\Delta \theta_0} - r_j (f'_j - \alpha) \right] \\ (\varphi_{\theta\theta})_{i,j,k} = \frac{2}{\Delta \theta_{-1}} \left[r_j (f'_j - \alpha) - \frac{\varphi_{i,j,l} - \varphi_{i,j,l-1}}{\Delta \theta_{-1}} \right] \end{cases} \quad (11)$$

(3) On the tail-trace plane, the pressure continuum and Kutta Condition are applied

$$(\varphi_{\theta})_{i,j,k} = \frac{1}{\Delta\theta_{,i}} \left[\frac{(\varphi_{i,j,i} - \Gamma_j) - \varphi_{i,j,i-1}}{\Delta\theta_{,i}} - \frac{\varphi_{i,j,i} - \varphi_{i,j,i-1}}{\Delta\theta_{,i}} \right] \quad (12)$$

Using the above finite-difference formulae, and on the plane of $i=\text{constant}$ and the straight live of $k=\text{constant}$, the algebraic simultaneous equations with $\varphi_{i,j-1,k}$, $\varphi_{i,j,k}$ and $\varphi_{i,j+1,k}$ as unknowns are established. These equations are three-diagonal and can be solved by the chase method. Assume the solution is $\hat{\varphi}_i$, then the solution after relaxation is

$$\varphi_i^{*+1} = \omega \hat{\varphi}_i^{*+1} + (1 - \omega) \varphi_i^* \quad (13)$$

where ω is the relaxation parameter. The subsonic relaxation parameter ω_s in the computation is selected as 1.9 or 0.9; the supersonic relaxation parameter ω_{λ} is selected as 0.9. The iteration method is conducted to solve for the entire flow field. The iteration stops when the entire flow field satisfies

$$|\varphi_{i,j,k}^{*+1} - \varphi_{i,j,k}^*| < \epsilon \quad (14)$$

where ϵ is the convergence range and is generally selected as $\epsilon = 0.1 \times 10^{-4}$.

The computation formula for pressure coefficient on wing is

$$C_p = -2\varphi_s \quad (15)$$

On the surface of the body, the second-order term of the horizontal disturbance velocity is reserved

$$C_p = -2\varphi_s - \left(\varphi_s^2 + \frac{1}{r^2} \varphi_s^2 \right) \quad (16)$$

II. Example

1. Wing-Body Combination Equation

(1) The wing is a rectangular wing with double-arc airfoil

$$z = \frac{2b}{b} \left(\frac{b^2}{4} - x \right) \quad (17)$$

The airfoil relative thickness ratio $\delta = 0.06$; chord length $b=1$ is a reference length; the aspect ratio $\lambda = L/b=5.4$; L is the span length including the body.

2. The Body is the Model "AGARD-B" Body, the Equation for the Contour of the Head is

$$R(x) = \frac{1}{3} (5D + x) \left[1 - \frac{1}{9} (5D + x)^2 + \frac{1}{54} (5D + x)^3 \right] \quad (18)$$

$(-5D \leq x \leq 2D)$

where D is the diameter of the cylindrical portion of the body. Assume $D=1$, when $x \geq 2$, then $R=0.5$ and extends into the downstream.

The origin of coordinates is selected at the intersection of the line connecting the center points of the chord and the body axes. The finite region of r is marked as I and the infinite region as II. The sampling points in the x , r (or η) and θ -direction are all distributed at nonequal distance.

III. computation Results

1. The maximum Mach number and attack angle in the computation region I are $M_{a\infty} = 0.926$ and $\alpha = 2^\circ$ respectively; in the computation region II they are $M_{a\infty} = 0.98$ and $\alpha = 4^\circ$ respectively. This indicates

that the coordinate conversion $\eta = br/(1+ar)$ in the r-direction can increase the range of the calculated Mach number and attack angle of the small-disturbance equation.

2. Figure 2 gives the comparison curves between the computed results and the two-variable test results at $M_{a\infty} = 0.965$, $\alpha = 2^\circ$ and $\tilde{y} = 0.5$ (\tilde{y} is the spanwise relative location on the wing cross-section). This figure shows that the computed results in region II are reasonable.

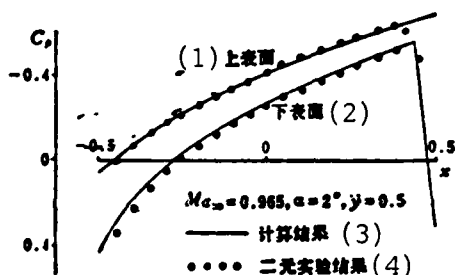


Fig. 2. Comparison between computed results and test results
Key: (1) upper surface; (2) lower surface; (3) computed results;
(4) two-dimensional test results.

3. Figure 3 shows that there is difference between the computed results of region I and II. At $\epsilon = 0.1 \times 10^{-4}$, when the $M_{a\infty}$ is larger, there is a difference in the chordwise distribution of wing surface pressure coefficients and it becomes more obvious near the wingtip. This is because the outer boundary of region I is like a wall, causing the local Mach number to increase and the absolute value of C_p on the upper surface to be larger and that for the lower surface to be smaller.

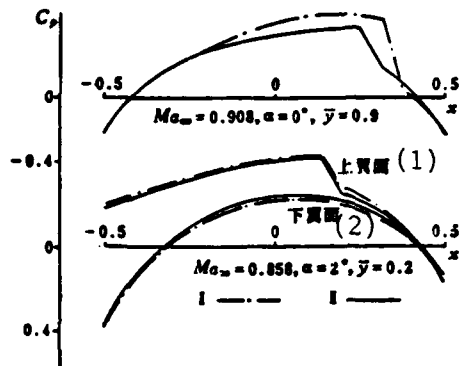


Fig. 3. Influence of computation regions on computed results
Key: (1) upper wing surface; (2) lower wing surface.

4. Figure 4 gives the curves of influence of subsonic relaxation parameters on computed results. Under the same \mathcal{E} , the computed results at $\omega_1=1.9$ is more accurate than that at $\omega_1=0.9$; its convergence rate is faster. There are similar phenomena in both computation region I and II. This indicates that, under guaranteed convergence condition, the larger ω_1 is selected (> 2), the faster the convergence rate of computation and the higher the accuracy of data.

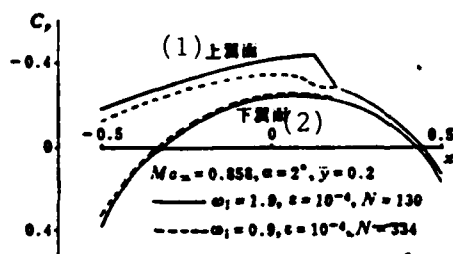


Fig. 4. Influence of relaxation parameters on computed results
Key: (1) upper wing surface; (2) lower wing surface.

REFERENCES

- (1) Knechtel, E. D. Experimental Investigation at Transonic Speeds of Pressure Distributions over Wedge and Circular-Arc Airfoil Sections and Evaluation of Perforated-Wall Interference. NASA TN D-16, (1959).

Abstract

A three-dimensional computation of a jet in a crossflow has been performed on a microcomputer. The SIMPLE method is adopted with some modifications. A special computer code is developed in conformity with the limited memories of the microcomputer. Velocity and pressure distributions are given and compared with the available experimental data satisfactorily.

NUMERICAL COMPUTATION OF THE THREE-DIMENSIONAL VISCOUS INTERFERENCE
FLOW FIELD OF A VERTICAL JET IN A CROSSFLOW

Pan Huachen and Zhang Shiyang
Nanjing Aeronautical Institute

Submitted 1 March 1985

A vertical jet shot out of a flat plate will interfere with a low speed incident flow parallel to the flat plate (crossflow), causing complex flow phenomena to occur. The jet is deflected by the crossflow, and its velocity is rapidly reduced; the incident flow is blocked and drawn by the jet (Fig. 1). The jet and the incident flow interact with each other causing two symmetrical vortex cores to develop under the jet.

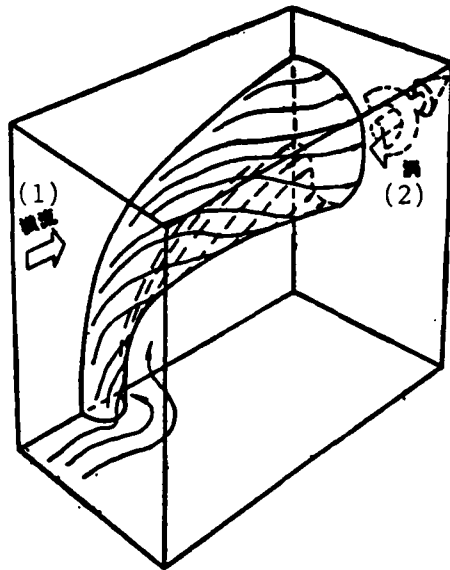


Fig. 1. Flow field of a vertical jet interferring with a crossflow and its computation domain
Key: (1) crossflow; (2) vortex.

The vortex caused by this interference develops along the direction of the wall surface and it can be used as a means to control the attach surface layer^[1]. It can also be applied to heat transfer engineering and other areas. There have been numerous experimental studies on this kind of flow both in our country and abroad^[1-4]. Due to the difficulties in measurement, it is generally difficult to obtain detailed data of the entire flow field, especially near the nozzle. It is impossible to conduct computation using two-dimensional or nonviscous method because of the complexity of the flow; the full three-dimensional viscous numerical computation method must be used. This kind of flow possesses strong three-dimensional mixing effects and needs to use appropriate turbulence model. According to the principles in References [6, 7], we developed a computer program and performed computation.

I. Basic Equations

The basic equation of a three-dimensional, steady, incompressible, time-averaged Reynold number turbulent flow in the rectangular coordinates is: continuity equation

$$\frac{\partial u_i}{\partial x_i} = 0 \quad (1)$$

The momentum equation (with the assumption of vortex viscosity)

$$\rho u_i \frac{\partial u_j}{\partial x_i} = -\frac{\partial p^*}{\partial x_j} + \frac{\partial}{\partial x_i} \left[\mu_e \left(\frac{\partial u_j}{\partial x_i} + \frac{\partial u_i}{\partial x_j} \right) \right] \quad (2)$$

where the effective viscosity μ_e is defined as

$$\mu_e = \mu_l + \mu_t \quad (3)$$

where μ_l is the laminar viscosity. μ_t is the turbulent viscosity and is determined by the following turbulence model

$$\mu_t = C_\mu \rho K^2 / \epsilon \quad (4)$$

where K is the turbulence kinetic energy. ϵ is the dissipation rate of K and is determined by the following equations

$$\rho u_i \frac{\partial K}{\partial x_i} = \frac{\partial}{\partial x_i} \left(\frac{\mu_t}{\sigma_k} \frac{\partial K}{\partial x_i} \right) + G - \rho \epsilon \quad (5)$$

$$\rho u_i \frac{\partial \epsilon}{\partial x_i} = \frac{\partial}{\partial x_i} \left(\frac{\mu_t}{\sigma_\epsilon} \frac{\partial \epsilon}{\partial x_i} \right) + (C_{1G} G - C_{2\rho} \rho \epsilon) \frac{\epsilon}{K} \quad (6)$$

where G is the generation rate of the turbulence kinetic energy

$$G = \mu_t \left(\frac{\partial u_i}{\partial x_j} + \frac{\partial u_j}{\partial x_i} \right) \frac{\partial u_i}{\partial x_j} \quad (7)$$

The coefficients used in the equations are adopted from the data recommended by Reference [8]:

$$C_\mu = 0.09, C_1 = 1.44, C_2 = 1.92, \sigma_k = 1, \sigma_\epsilon = 1.3 \quad (8)$$

Since the above turbulence model is used, p^* in Equation (2) is

$$p^* = p + \frac{2}{3} \rho K$$

where $2/3$ K can be regarded as turbulent pressure term.

II. Solution Method

The method used by this paper is based primarily upon the SIMPLE method^[7]. Said method adopts the iteration solution method. The three velocity components u , v and w used to solve the x-direction momentum equation are all old values; u used to solve the y-direction momentum equation is a new value; and u and v used to solve the z-direction momentum equation are new values. It was found during actual computation that this kind of nonconforming value character was an important factor which caused divergence in solving the equation. Therefore, when we were developing the program the newly obtained u and v values were temporarily stored and old u , v and w values were used to perform iteration for all three momentum equations, thereby guaranteeing the conforming value character.

In order to increase efficiency and lower cost, the existing INTEL-86-330 microcomputer was adopted to perform computation. Said program requires more memory. The example in this paper requires more than 100 giga bytes in memory at least, and the available memory space of the said microcomputer is only a little more than 100 K. Therefore, during the development of the program the technique of exchanging with secondary storage was adopted. Every three-dimensional group was divided into a dozen or so two-dimensional group and stored in hard disk. During computation they were called in separately by a subroutine to take part in the iteration and then restored. This greatly saved memory space. Yet as a price, the computation speed dropped about 20 fold.

III. Example

The experimental conditions in Reference [3] for the incident flow and geometric data are used. The incident flow velocity is 39 m/sec and jet velocity is 156 m/sec with a velocity ratio of 4. The symmetry of flow field only considers half of the flow field cut by the symmetric plane, as shown in Fig. 1. The computation domain is a box-shaped region with its bottom connected to the flat plate. One of the sides is the symmetric plane and the other four sides are the upstream, downstream boundaries and infinite boundaries, respectively. The grid is in the form of rectangular coordinates: x-direction (flow direction) has 20 rows of grid, z-direction (perpendicular to the plate) has 16 rows and y-direction has 12 rows for a total of 3840 grid points (measurement points). In order to properly simulate the details of flow field near the jet nozzle, a variable spacing grid is used to give dense grid near the jet nozzle and sparse grid for further flow field. Using the nozzle diameter D as the reference, the upstream boundary is $3.5 D$ from the center of the nozzle and the downstream boundary is $8 D$ from the center of the nozzle. The z-direction infinite boundary is about $12 D$ from the plate and the side infinite boundary is about $5 D$ from the symmetric plane. The method in Reference [6] is adopted. Six grid points are used to simulate a semi-circle jet nozzle. Meanwhile the total area corresponding to the six grid points is made to be in agreement with the area of the semi-circle jet nozzle.

The upstream boundary defines the incident flow velocity. The normal velocities on the infinite boundary, the symmetric plane boundary and the flat plate are all assumed to be zero. The jet velocity is defined by the jet nozzle. The gradient of the tangential velocities v and w on the downstream boundary are assumed to be zero, yet u is adjusted according to the total flow rate on the basis of its value on the previous row. The wall surface is processed by adopting the wall surface function method^[8].

The standard for computation convergence is set at when both the corresponding remainders of the momentum and continuity equations reach 5%. This example required 90 steps and spent 170 hours on the microcomputer.

V. Results and Their Discussions

In order to verify the computation, the results are compared with the test data of Reference [3, 4, 5]. Figure 2 shows the velocity contours on the symmetric plane. In the figure, the line with indexing points is the jet center line drawn by using the peaks of the contours, and it can be seen that the line is in good agreement with the test data. See Fig. 3 for the decay of jet velocity. In the figure, W_{\max} is the jet velocity at the jet nozzle, s is the natural coordinates along the jet, W_j is the jet velocity along s . The computed velocity decays faster than the test value, but the difference is not distinctive and both show that the rate of velocity decay follows a rule of first small, then large, and again from large back to small. Figure 4 is the projection of vortex core contour on the symmetric

plane. The vortex core trace derived from the computed values is more complicated. The low pressure centers basically coincide with the vortex core contour, otherwise the centripetal force that makes the air streamlines turn vortically will not be generated. The curve in Fig. 4 is the projection of the low pressure centers on the symmetric plane, i.e., the approximation of the vortex core contour, and matches well with the vortex core test values. Figure 5 is the comparison of computed values (left half) and test values (right half) of the pressure coefficient distributions on the flat plate. Judging from the trend of pressure distributions, the computed values of pressure rise behind the jet nozzle on the flat plate are faster than the test values.

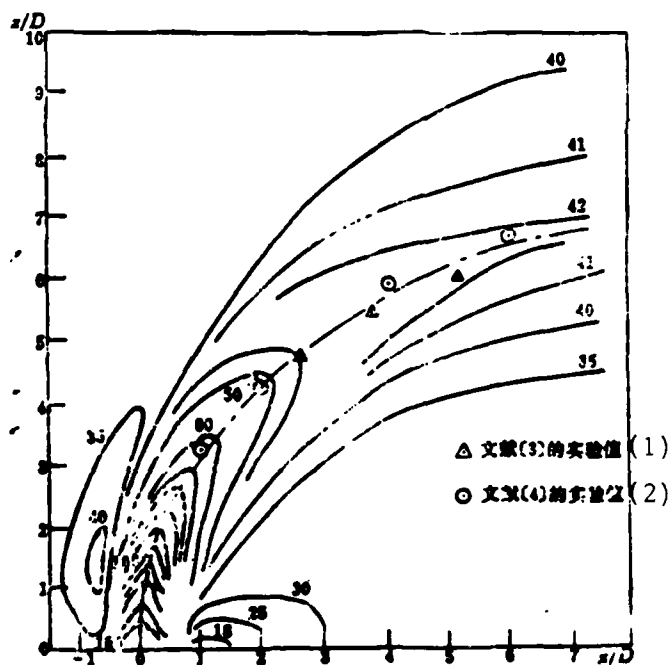


Fig. 2. Velocity distributions and the location of jet center line on the symmetric plane
 Key: (1) test values of Reference [3]; (2) test values of Reference [4].

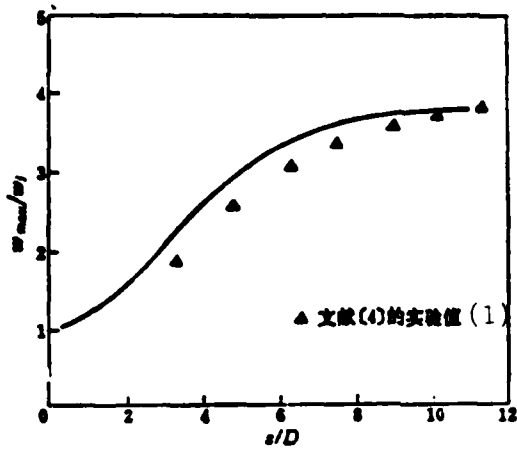


Fig. 3. Rule of velocity decay on the jet center line
 Key: (1) test values of Reference [4].

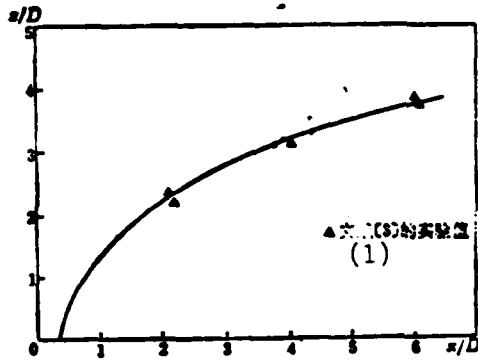


Fig. 4. Projection of the location of vortex core on the symmetric plane
 Key: (1) test values of Reference [3].

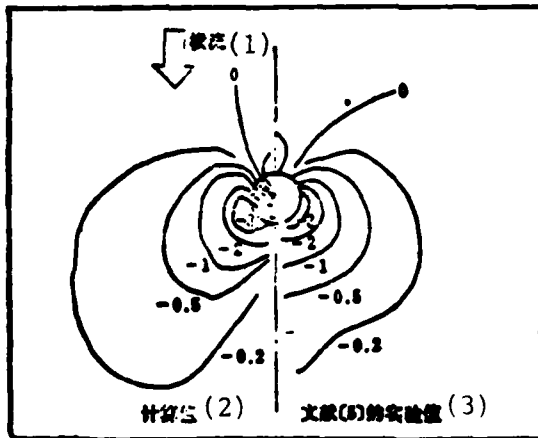


Fig. 5. Pressure coefficient distribution on the flat plate
 Key: (1) Crossflow; (2) Computed values; (3) test values of Reference [5].

The three-dimensional viscous flow computation method introduced by this paper can compute detailed data of the interference flow field of a vertical jet in an incident flow. The comparison with test results shows that the computed results are more accurate, especially the locations of jet contour, vortex core contour, etc. The fact that the computed jet decay is a little faster and the computed pressure rise behind the jet nozzle is faster indicates that the numerical dissipation might be larger, but not enough to cause significant influence on the prediction of the entire flow field. Therefore, the said numerical method can be an effective tool for analyzing flow field.

REFERENCES

- [1] Zhang Shiyong and Li Fang, An experimental Study on Air Vortical Flow Machine, ACTA Aeronautica Et Astronautica Sinica, No. 4, 1984, p. 425.
- [2] Li Fang, Vortex of the Air Vortical Flow Machine, Master's degree theses, Nanjing Aeronautical Institute, 1982.
- [3] Frann, R. & Weston, R., Induced Velocity Field of a Jet in a Crossflow, NASA TP 1087, (1978).
- [4] Chassaing, P. et al., Physical Characteristics of Subsonic Jet in a Cross Stream, J. of Flu. Mech., Vol 62, Part 1 (1974), p41.
- [5] Mosher, D., An Experimental Investigation of a Turbulent Jet in a Cross Flow, Report 70-7, Georgia Inst. of Tech., (1970).
- [6] Patankar, S. et al., Prediction of the 3-dimensional Velocity Field of a Deflected Turbulent Jet, Trans. ASME, J. Flu. Eng. Dec. (1977), p758.
- [7] Patankar, S., Numerical Heat Transfer & Fluid Flow, Hemisphere Publishing Corporation, (1980).
- [8] Launder, B. & Spalding, D., The Numerical Prediction of Turbulent Flows, Computer Method in Applied Mech. & Eng., Vol. 3 (1974), p263.

DISTRIBUTION LIST
DISTRIBUTION DIRECT TO RECIPIENT

<u>ORGANIZATION</u>	<u>MICROFICHE</u>
A205 DMAHTC	1
A210 DMAAC	1
B344 DIA/RTS-2C	9
C043 USAMIA	1
C500 TRADOC	1
C509 BALLISTIC RES LAB	1
C510 R&T LABS/AVRADCOM	1
C513 ARADCOM	1
C535 AVRADCOM/TSARCOM	1
C539 TRASANA	1
C591 FSTC	4
C619 MIA REDSTONE	1
D008 NISC	1
E053 HQ USAF/INET	1
E404 AEDC/DOF	1
E408 AFVL	1
E410 AD/IND	1
E429 SD/IND	1
P005 DOE/ISA/DDI	1
P050 CIA/OCR/ADD/SD	2
AFIT/LDE	1
FTD	
CCN	1
NLA/PHS	1
LLNL/Code L-389	1
NASA/NST-44	1
NSA/1213/TDL	2
ASD/FTD/QIA	1

END

11-86

DTIC